Sea Surface Kinematics From Near-Nadir Radar Measurements

Frédéric Nouguier, Bertrand Chapron, Fabrice Collard, Alexis A. Mouche, Nicolas Rascle, Fabrice Ardhuin, and Xiaoqing Wu

***Abstract*— Doppler radars at all incidence angles measure mean velocities and spreads that have complex relations to oceanic motions, with opportunities to measure winds, waves, and currents. Here, we extend previous theoretical models of backscatter and Doppler using a Kirchhoff approximation and the physical optics model. We show that in Ka-band, around 12° incidence, range-resolved measurements of Doppler and backscatter provide unambiguous estimations of the wave spectrum and surface current. This property is illustrated with numerical examples and airborne data from the Air Surface Water Ocean Topography instrument. The same measurement conditions can be exploited for global ocean mapping from the low Earth orbit sensor satellite configuration.**

***Index Terms*— Current, Doppler, microwave remote sensing, surface kinematics multiscale (SKIM) concept, Surface Water Ocean Topography (SWOT) Mission.**

I. Introduction

DOPPLER frequency anomalies, i.e., the difference between the measured and geometrically predicted Doppler frequencies, can provide local instantaneous line-of-sight (LOS) surface velocities from airborne and satelliteborne radar measurements over ocean scenes [1]–[3]. These velocities are governed by the distributed dispersion of the detected ocean surface wave scatterers and thus linked to the properties of local waves [4], [5] and current [6], [7].

Doppler anomalies thus provide direct ocean surface velocity measurements from space, possibly performing better than altimetry for small-scale currents, as neither a gradient of the measured quantity nor a relationship between sea level and current is assumed.

Yet, sensor physics and optimal instrumental configurations (incidence angle, wavelength, and polarization) are still to be clarified for the analysis of present measurements and the design of future satellite missions [8]. Indeed, these direct surface velocity measurements relate to detected scatter motions, including both orbital and surface current velocities. With that goal in mind, we consider, here, the particular case of a near-nadir configuration for a radar instrument operating at high frequency (Ka-band). In that case, the Kirchhoff asymptotic electromagnetic model framework [9] is sufficient [2], [10]. A key point is that a Kirchhoff integral operates as a harmonic filter at a selected resonant directional wavenumber $\boldsymbol{Q_H}$ of the joint characteristic function of the random surface elevations. This property follows from invariance by the translation of the scattering cross section. It follows that a zero-mean time-varying sea surface produces measurable phase shifts directly associated with the time derivative of this joint characteristic function. Under near Gaussian statistics, the phase shifts are the functions of moments of the surface elevation spectrum.

As derived in Section II, asymptotic analytical solutions provide the expected statistical properties of both the normalized radar cross section and its associated Doppler frequency. These developments are further discussed in Section III for radar measurements highly resolved in the range direction. In such a real-aperture-radar imaging configuration, time-varying complex reflectivity modulations emerge depending on the range-resolved ocean wave direction. Combined to mean complex reflectivity measurements dominated by wind-dependent short waves, this gives a quantitative knowledge of the ambient sea state conditions, namely long wave directional spectral properties and kinematics. The present developments extend previous analysis [11]–[13] to time-varying ocean surfaces. Combined range-resolved radar cross section and Doppler anomalies further open new strategies to separate wave-induced motions and surface current. Analytical solutions are then compared with near-nadir, highly resolved, Ka-band Doppler airborne measurements in Section IV. Conclusions follow in Section V.

II. Scattering Model and Doppler Evaluation

A. Basic Equations

The covariance of scattered fields (see [2], [14]) is expressed as

$$C(\tau) = \langle \boldsymbol{E}(\boldsymbol{K}, t)\boldsymbol{E}^*(\boldsymbol{K}, t+\tau)\rangle \tag{1}$$

where τ is the time lag and $\boldsymbol{K}$ is the electromagnetic wavenumber. The $\langle\cdot\rangle$ operator represents a spatial averaging and the star superscript stands for the complex conjugate. For near-nadir geometry and sufficiently high electromagnetic microwave frequency, i.e., Ku- or Ka-band, polarization effects can be ignored, and the Kirchhoff assumption (KA) provides adequate scattering asymptotic solutions.

Manuscript received September 22, 2017; revised February 9, 2018; accepted April 10, 2018. This work was supported in part by CNES under the SWOT Preparation Program, in part by LabexMer under Grant ANR-10-LABX-19-01, and in part by the TOSCA Program (COWS). *(Corresponding author: Frédéric Nouguier.)*

F. Nouguier, B. Chapron, A. A. Mouche, N. Rascle, and F. Ardhuin are with the Laboratoire d'Océanographie Physique et Spatiale, Université de Brest, CNRS, Institut Francais de Recherche pour l'Exploitation de la Mer, IRD, 29280 Plouzané, France (e-mail: frederic.nouguier@ifremer.fr).

F. Collard is with the Research Department, OceanDataLab, 29280 Locmaria-Plouzané, France.

X. Wu is with the Jet Propulsion Laboratory, California Institute of Technology, National Aeronautics and Space Administration, Pasadena, CA 91109 USA.

Color versions of one or more of the figures in this paper are available online at http://ieeexplore.ieee.org.

Digital Object Identifier 10.1109/TGRS.2018.2833200

Denoting $\boldsymbol{K}_0$ and $\boldsymbol{K}$, the incident and scattered EM wave vectors, with their respective horizontal $\boldsymbol{k}_0$, and $\boldsymbol{k}$ and vertical $-q_0$, and q components, one has

$$\boldsymbol{K}_0 = \boldsymbol{k}_0 - q_0\widehat{\boldsymbol{z}}, \quad \boldsymbol{K} = \boldsymbol{k} + q\widehat{\boldsymbol{z}} \tag{2}$$

with positive q and q_0 given by $k_0^2 + q_0^2 = k^2 + q^2 = K_0^2$. The Ewald vector is defined as $\boldsymbol{Q} = \boldsymbol{K} - \boldsymbol{K}_0$ with horizontal $\boldsymbol{Q_H} = \boldsymbol{k} - \boldsymbol{k_0}$ and vertical $Q_z = q + q_0$ components.

Under the KA, the electric scattered field writes $\boldsymbol{E}_{KA} = -ie^{iKR}\boldsymbol{E}_0\mathbb{S}(\boldsymbol{K})/R$, where $\boldsymbol{E}_0$ is the incident field amplitude, R is the distance between the satellite and the ground in the beam center, and $\mathbb{S}$ is the scattering matrix

$$\mathbb{S}(\boldsymbol{K}, t) = \frac{\mathcal{K}}{Q_z(2\pi)^2}\int_A \mathbf{dr}\ e^{i\boldsymbol{Q_H}\cdot\boldsymbol{r}}\ e^{iQ_z\eta(\boldsymbol{r},t)} \tag{3}$$

with A being the illuminated area at time t, $\mathcal{K}$ being the Kirchhoff kernel [15], and η being the sea surface elevation. Equation (1) then writes

$$C(\tau) \propto \iint_{A,A} e^{i\boldsymbol{Q_H}\cdot(\boldsymbol{r}'-\boldsymbol{r})}\langle e^{iQ_z(\eta(\boldsymbol{r}',t+\tau)-\eta(\boldsymbol{r},t))}\rangle d\boldsymbol{r}d\boldsymbol{r}'. \tag{4}$$

B. Mean Doppler Frequency

Assuming that the instrument motion relative to the solid Earth is accurately evaluated, the remaining mean geophysical Doppler (GD) frequency f_{GD} can be defined as [3]

$$2\pi f_{\mathrm{GD}} = -i\partial_\tau C(0)/C(0) \tag{5}$$

where, from now on, ∂_α is the derivation relative to α variable, $\widehat{\boldsymbol{x}}$ is the ground range direction, and $\widehat{\boldsymbol{y}}$ is the ground azimuth direction, so that $\boldsymbol{Q_H} = -Q_H\widehat{\boldsymbol{x}}$. Considering $(\boldsymbol{r}', t+\tau) = (\boldsymbol{r}+\boldsymbol{\xi}, t+\tau)$ and homogeneous Gaussian statistics for the sea surface elevation, (5) becomes

$$2\pi f_{GD} = -i\partial_\tau\zeta^0/\zeta^0 \tag{6}$$

where

$$\zeta(\tau) = \int_A e^{i\boldsymbol{Q_H}\cdot\boldsymbol{\xi}}e^{-Q_z^2(\rho(0,0)-\rho(\boldsymbol{\xi},\tau))}d\boldsymbol{\xi}. \tag{7}$$

The range component of $\boldsymbol{\xi}$ is ξ_x, and ρ is the spatio-temporal surface elevation correlation function whose expression can be found in Appendix A. In (7), $\boldsymbol{Q}_H$ and Q_z dependence is implicit in the definition of ζ, and the zero superscript corresponds to quantity taken at $\tau = 0$ as

$$\zeta^0 = \zeta(\boldsymbol{Q}_H, Q_z, 0) \quad \text{and } \partial_\tau\zeta^0 = \left.\frac{\partial\zeta(\boldsymbol{Q}_H, Q_z, \tau)}{\partial\tau}\right|_{\tau=0}.$$

The correlation function can be expanded as

$$\rho(\boldsymbol{\xi}, \tau) \simeq \rho(\boldsymbol{\xi}, 0) + \partial_t\rho(\boldsymbol{\xi}, 0)\tau \tag{8}$$

$$\simeq \rho(\boldsymbol{\xi}, 0) + \mathbf{msv}\cdot\boldsymbol{\xi}\tau \tag{9}$$

introducing the mean slope speed vector

$$\mathbf{msv} = (\mathrm{mss}_{\mathrm{xt}}, \mathrm{mss}_{\mathrm{yt}}) = \partial_\tau\nabla_{\boldsymbol{\xi}}\rho(0,0) \tag{10}$$

with the definition of all mean squared quantities

$$\mathrm{mss}_{x^\alpha y^\beta t^\gamma} = 2\int_{\mathbb{R}^2} k_x^\alpha k_y^\beta\omega^\gamma\, S_d(\boldsymbol{k})\ d\boldsymbol{k} \tag{11}$$

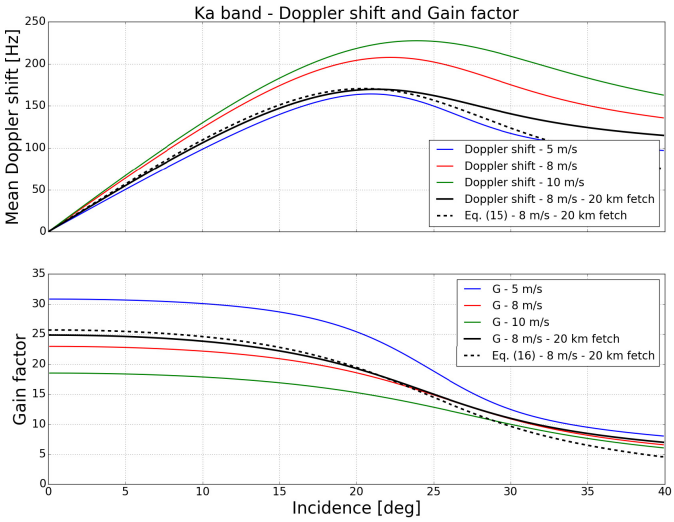

Fig. 1. (Top) Mean Doppler frequency shift and (Bottom) gain factor in upwind looking direction versus incidence angle. In both figures, blue, red, and green curves, respectively, correspond to 5-, 8-, and 10-m/s wind speed Elfouhaily spectrum with infinite fetch. Black curves correspond to a 8-m/s wind speed Elfouhaily spectrum with a 20-km long fetch ($\lambda_{\mathrm{peak}} \approx 45$ m). Black solid curves are for Kirchhoff assumption (KA) labeled (6) and black dashed curves for (15).

from spectral moments of S_d, the directional (i.e., single-sided) ocean elevation spectrum (see Appendix A for details). We recall that in (11), x and y components are, respectively, the range and azimuth ones. Substituting (9) into (6) leads to

$$2\pi f_{\mathrm{GD}} = Q_z^2\ \mathbf{msv}\cdot\nabla_{\boldsymbol{Q_H}}\zeta^0/\zeta^0 \tag{12}$$

where the $\boldsymbol{Q_H}$ derivation has to be done at constant Q_z.

Following, the radar cross section writes:

$$\sigma^0 = \frac{1}{\pi}\frac{|\mathcal{K}|^2}{(2K)^2}\sec^2(\theta)\zeta^0 \tag{13}$$

with θ being the incidence angle. The ζ^0 term brings an additional $\sec^2(\theta)$ dependence. To ease the development, let us introduce $\psi^0 = \cos^4(\theta)\sigma^0$. Note, in (12), the $\boldsymbol{Q_H}$ differentiation at constant Q_z cannot be directly derived. However, since close to nadir incidence, $\cos(\theta)$ has small variations, we can simplify

$$\nabla_{\boldsymbol{Q_H}\cdot|Q_z} \approx \left|\begin{matrix} Q_z^{-1}\partial_{\tan\theta}\cdot \\ Q_H^{-1}\partial_\varphi\cdot \end{matrix}\right|_K \tag{14}$$

where φ is the azimuthal angle. It gives

$$f_{\mathrm{GD}} = \frac{Q_z}{2\pi}\left(\mathrm{mss}_{\mathrm{xt}}\frac{\partial_{\tan\theta}\psi^0}{\psi^0} + \frac{\mathrm{mss}_{\mathrm{yt}}}{\tan\theta}\frac{\partial_\varphi\psi^0}{\psi^0}\right). \tag{15}$$

It clearly highlights that the mean Doppler shift is directly weighted by the rates of variations of the radar cross section with both incidence and azimuth. Fig. 1 (top) shows the expected mean Ka-band Doppler shift frequency versus incidence, using a 20-km fetch and 8-m·s^{-1} wind speed Elfouhaily spectrum [16], in an upwind configuration (black curve). Fig. 2 shows its azimuthal dependence at 12° incidence. In Figs. 1 and 2, the approximation given by (15) is plotted as the black dashed curve. Doppler shifts for fully developed

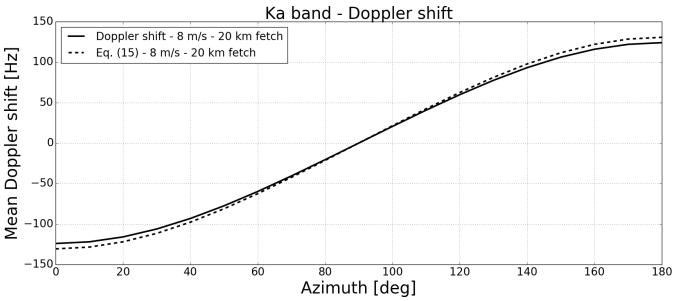

Fig. 2. Mean Doppler frequency shift at a 12° incidence versus azimuth angle. Curves correspond to a 8-m/s wind speed Elfouhaily spectrum with a 20-km long fetch ($\lambda_{\text{peak}} \approx 45$ m). Black solid curve is for Kirchhoff assumption (KA) labeled (6) and black dashed curves for (15).

wind sea with Elfouhaily spectrum at 5-, 8-, and 10-m/s wind speeds are also superimposed in Fig. 1.

The second term in (15) is governed by the relative azimuthal sensibility of the radar cross section weighted by the mean slope speed in the azimuthal direction mss_{yt}. The azimuthal variability of the radar cross section is usually expanded in a harmonic form having extrema in up-, down-, and cross-wind directions [17], [18]. The second term in (15) thus vanishes for these particular directions.

We note that for linear waves $\text{mss}_{\text{xt}} = (1/2)\boldsymbol{U}_S^{\infty} \cdot \widehat{\boldsymbol{x}}$, where $\boldsymbol{U}_S^{\infty}$ is the surface Stokes drift velocity of deep water waves. In upwind and downwind configurations and for geophysical purposes, it is convenient to use the nondimensional gain factor G introduced in [1]

$$G = -\frac{1}{2}\frac{2\pi f_{\text{GD}}}{Q_H \text{mss}_{\text{xt}}} \approx \frac{-1}{2\tan(\theta)}\left(\frac{\partial_{\tan\theta}\psi^0}{\psi^0}\right). \tag{16}$$

The negative factor $-(1/2)$ accounts for the relation between mss_{xt} and the Stokes drift and further ensures a positive value of G. Fig. 1 (bottom) shows the gain factor G versus incidence in upwind configuration for the same situations of the top panel. The gain factor is almost independent of the azimuthal angle.

Close to nadir, up to about 20° and for all azimuth, (15) well approximates a full KA solution for the expected mean Doppler shift frequency.

In the Ka-band radar data collected during the Southern Ocean Waves Experiment [19], the departure of the radar cross section measurements from a Gaussian shape approximation was reported as

$$\ln\left(\frac{\cos^4(\theta)\sigma^0}{\sigma^0_{\text{max}}}\right) = -A\tan^2(\theta) + B\tan^4(\theta). \tag{17}$$

Except for light wind speed, a robust relationship writes

$$B = 0.5676\ A^{1.332}. \tag{18}$$

The $\tan^2(\theta)$ rate of change A identifies with $1/\text{mss}_{\text{shape}}$ as derived in [10] from the Ka-band satellite measurements of the dual-frequency precipitation radar on-board the Global Precipitation Measurements core [20]. For wind speed of about 7 m/s with 1.5-m significant wave height, it gives

$$\begin{cases} A = \text{mss}_{\text{shape}}^{-1} \approx 33 \\ B \approx 60 \\ \left.\dfrac{\partial_{\tan\theta}\psi^0}{\psi^0}\right|_{\theta=12^\circ} \approx -11.7. \end{cases} \tag{19}$$

A typical upwind mss_{xt} derived from a fully developed Elfouhaily spectrum at 7-m $\cdot$ s^{-1} wind speed is $\text{mss}_{xt} \approx -0.054$ m $\cdot$ s^{-1}, leading to a Doppler shift frequency $f_{\text{GD}} \approx 155$ Hz at 12° incidence. At this wind speed, the additional B term tends to decrease the $\partial_{\tan\theta}\psi^0/\psi^0$ term. A parabolic approximation of the $\cos^4(\theta)\sigma^0$ incidence falloff would have then led to a 20% overestimation of the Doppler shift, i.e., about 30 Hz translating to a 12-cm $\cdot$ s^{-1} LOS velocity difference.

C. Sea Surface Current Doppler Shift

An additional horizontal current vector $\boldsymbol{U} = (U_x, U_y)$, vertically uniform with depth, modifies the surface wave dispersion

$$\omega = \sqrt{g|\boldsymbol{k}|\left(1 + |\boldsymbol{k}|^2/k_M^2\right)} + \boldsymbol{k}\cdot\boldsymbol{U} \tag{20}$$

where $\boldsymbol{k}$ is the wavenumber vector and $k_M = 363.2$ rad.m^{-1} is the wave vector corresponding to the gravity-capillary transition regime defining waves traveling with minimum phase velocity.

As shown in Appendix A, the correlation function of the surface elevations simply becomes

$$\rho_c(\boldsymbol{\xi}, \tau) = \rho(\boldsymbol{\xi} - \boldsymbol{U}\tau, \tau). \tag{21}$$

Substituting (21) into (7), we now have

$$\zeta_c(\tau) = e^{-iQ_H U_x}\zeta(\tau) \tag{22}$$

$$f_C = \frac{Q_H}{2\pi}U_x = \frac{2\sin(\theta)}{\lambda_{\text{em}}}U_x \tag{23}$$

where f_c is the additional current frequency shift with λ_{em} being the electromagnetic wavelength ($\lambda_{\text{em}} \approx 8$ mm in Ka-band). In deriving the present asymptotic expression, the surface current contribution straightforwardly results from the modification of the wave dispersion relationship. Mathematically, the surface current modifies the wave vertical velocities $\partial_t\eta$ and thus appears through the vertical Q_z factor in (7). This authorizes the change of variable (21), which acts to transform the modified vertical contribution onto a horizontal effect. Without change of variable and keeping the current impact on the vertical terms, the correlation function expansion (9) would be modified to also lead to (23).

At 12° incidence, a 50-cm $\cdot$ s^{-1} horizontal current, in the radar looking direction, then corresponds to an additional 26-Hz Doppler shift. Compared with the expected large background Doppler bias, a precise knowledge of the ambient sea state in terms of both long waves and wind-dependent short waves is thus an essential requisite for an accurate estimation of the current velocity.

III. Range-Resolved Measurements

To mitigate this difficulty, the dependence of Doppler and normalized radar cross section (NRCS) measurements on the sea state has first been expressed as a function of wind speed and direction [8], [21], [22]. Indeed, the wave-induced Doppler bias is dominated by wind seas and largely minimized for cross-wind radar measurements to favor surface current estimates. Building on multiple azimuth and incidence angle observations, practical algorithms can be proposed [23]. Still, the expected root mean square variability of U_S^∞ for a given wind speed is 40% [5]. Hereafter, a complementary approach is exposed. It builds on the range-resolved measurements for the exploitation of the detected radar signal modulations in order to more precisely characterize the ambient sea state. Of particular interest for our purpose, this provides a direct estimate of $\boldsymbol{U}_S^\infty$ that is more accurate than an empirical wind-based algorithm.

A. Modified Basic Equations for Range-Resolved Measurements

Resolution in the range ($\widehat{\boldsymbol{x}}$) direction can be achieved by the convolution of the received and flipped emitted chirps, possibly leading to a fine resolution in the LOS (e.g., 3 m projected on the ground for a 250-MHz bandwidth under satellite configuration). For each range gate, an estimation of (4) follows as:

$$\widetilde{C}(x,\tau) \propto \iint_{A,A} e^{i\boldsymbol{Q_H}\cdot\boldsymbol{\xi}} \langle e^{iQ_z\eta'_u - iQ_z\eta_u}\rangle e^{iQ_z(\eta'_r-\eta_r)} d\boldsymbol{r}d\boldsymbol{\xi} \quad (24)$$

where the subscript "r" stands for the resolved surface profile and the subscript "u" stands for the unresolved surface profile ($\eta = \eta_r + \eta_u$). The resolved and unresolved wave scales are thus directly related to the gate shape and its orientation. The spatial integration is now performed over the resolved cell area A. Expansion in space and time gives

$$\eta'_r(\boldsymbol{r}+\boldsymbol{\xi}, t+\tau) = \eta_r + \nabla\eta_r\cdot\boldsymbol{\xi} + \partial_t\eta_r\tau \quad (25)$$

which yields

$$\widetilde{C}(x,\tau) \propto \iint_{A,A} e^{iQ_z\partial_t\eta_r\tau + iQ_z\nabla\eta_r\cdot\boldsymbol{\xi}} d\boldsymbol{r} \times e^{i\boldsymbol{Q_H}\cdot\boldsymbol{\xi}}\langle e^{iQ_z(\eta'_u-\eta_u)}\rangle d\boldsymbol{\xi}. \quad (26)$$

The intercepted area in the cross-LOS or azimuth direction L_y is still very large, i.e., order of km, constrained by the antenna pattern. Assuming that $\partial_t\eta_r$ and $\nabla\eta_r$ are Gaussian processes, evaluation of the along-azimuth integral in (26) leads to

$$A\exp\left[iQ_z\overline{\partial_t\eta_r}(x)\tau + iQ_z\overline{\partial_x\eta_r}(x)\xi_x\right] \times \langle e^{iQ_z(\eta'_r-\eta_r)}\rangle \quad (27)$$

where $\overline{\partial_t\eta_r}(x)$ and $\overline{\partial_x\eta_r}(x)$ are the residual mean values of $\partial_t\eta_r$ and $\nabla\eta_r$, respectively, integrated over the azimuth at a given x position (gate position) and implicit time t. Their expressions are not straightforward and given in Appendix B. To leading order, these residual mean azimuthal profiles, $\overline{\partial_t\eta_r}(x)$ and $\overline{\partial_x\eta_r}(x)$, depend on the azimuthal aperture, with residual variances increasing with their distributed azimuthal correlation lengths, and decreasing as L_y^{-1}. Also note that the cross-LOS surface gradient has a much shorter correlation length in the azimuthal direction, and its residual mean can be neglected, i.e., $\overline{\partial_y\eta_r}(x)$=0.

Substituting (27) into (26), and having again $\boldsymbol{Q_H} = -Q_H\hat{\boldsymbol{x}}$, we find

$$\widetilde{C}(x,\tau) \propto Ae^{iQ_z\overline{\partial_t\eta_r}(x)\tau} \times \widetilde{\zeta}(x,\tau) \quad (28)$$

where

$$\widetilde{\zeta}(x,\tau) = \int_A e^{i(Q_z\overline{\partial_x\eta_r}(x) - Q_H)\xi_x} e^{-Q_z^2(\rho(0,0)-\rho(\boldsymbol{\xi},\tau))} d\xi_x d\xi_y \quad (29)$$

recognized as the spatio-temporal Kirchhoff integral with an additional $Q_z\overline{\partial_x\eta_r}(x)$ phase term, correcting the initial resonant frequency Q_H. The range-resolved Doppler shift frequency then writes

$$2\pi\,\widetilde{f}_{GD}(x) = -i\frac{\partial_\tau\widetilde{C}(x,0)}{\widetilde{C}(x,0)}. \quad (30)$$

B. NRCS and Doppler Modulations

Range-resolved measurements thus provide both the NRCS and Doppler at each gate. In particular, $\widetilde{\sigma}^0(x) \propto \sec^2(\theta)\widetilde{\zeta}^0(x)$, and assuming the overall tilting modulation by resolved waves in (29) to be sufficiently small, it simply comes

$$\widetilde{\psi}^0(x) = \psi^0 - \overline{\partial_x\eta_r}(x)\partial_{\tan\theta}\psi^0. \quad (31)$$

Using the same derivations as in Section II-B, the resulting Doppler shift associated with a given gate, at distance x and time t, writes

$$2\pi\,\widetilde{f}_{\mathrm{GD}}(x) = Q_z\overline{\partial_t\eta_r}(x) + Q_z^2\mathbf{msv}\cdot\nabla_{\boldsymbol{Q_H}}\widetilde{\zeta}^0(x)/\widetilde{\zeta}^0(x) \quad (32)$$

and further approximated in up/downwave configuration

$$2\pi\,\widetilde{f}_{\mathrm{GD}}(x) = Q_z\overline{\partial_t\eta_r}(x) + \frac{Q_z\mathrm{mss_{xt}}}{\widetilde{\psi}^0(x)}\left[\partial_{\tan\theta}\psi^0 - \overline{\partial_x\eta_r}(x)\partial^2_{\tan^2\theta}\psi^0\right] \quad (33)$$

where $\overline{\partial_t\eta_r}(x)$ and $\overline{\partial_x\eta_r}(x)$ are the space- and time-dependent mean azimuthal velocity and slope of the resolved long wave profile.

C. Numerical Simulation

To illustrate these results, a numerical simulation is performed. A random Gaussian sea surface is simulated [24] and shown in Fig. 3. The surface is generated from an Elfouhaily spectrum corresponding to a 20-km fetch and 8-m $\cdot$ s^{-1} wind speed condition, leading to a wind sea system with a 45-m peak wavelength. Such a sea state corresponds to environmental conditions discussed in Section IV. A 5-m ground resolution is assumed in the radar LOS in the upwind direction. The generated surface is sampled at a 2.5-m resolution. Samples of the mean azimuthal profiles of the surface slope in the range direction and the surface vertical velocities are shown in Fig. 4. Azimuthal averaging is realized over 1280 m. NRCS as well as Doppler modulations are estimated through the full Kirchhoff approximation [see (30)] and the approximate

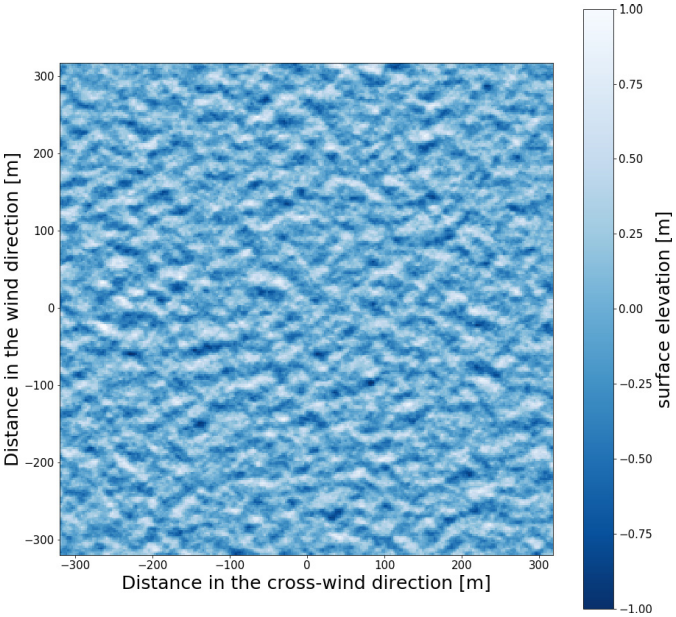

Fig. 3. 640 m × 640 m patch extracted from a larger random 2560 m × 1280 m Gaussian sea surface. A 2.5-m sampling is used in both horizontal directions. Elfouhaily spectrum with a 20-km fetch at a 8- $\mathrm{m \cdot s^{-1}}$ wind speed is used. The peak wavelength is about 45 m. Color scale is in meter.

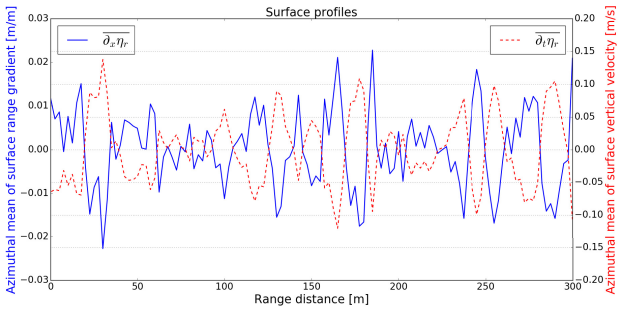

Fig. 4. Mean azimuthal profiles of the surface slope in the range direction and the surface vertical velocities. Averaging azimuthal length is 1280 m.

equations (31) and (33). Fig. 5 shows the Ka-band signal modulations at 12° incidence. A very satisfying agreement between both the methods is obtained. From now on, we use (31) for NRCS modulations and (33) for Doppler shift modulations.

Equation (31) shows that, at a given incidence angle (ψ^0 and $\partial_{\tan\theta}\psi^0$ are constants), the NRCS modulation spectra is directly proportional to the surface LOS slope ($\overline{\partial_x \eta}$) spectrum. Fig. 6 compares normalized NRCS modulation spectra obtained at 6°, 8°, and 12° incidence with the spectrum of the LOS mean surface slope profile ($\overline{\partial_x \eta}$). All spectra are thus well superimposed. Such a principle is at the heart of the concept of the on-board SWIM wave scatterometer on the China-France Ocean SATellite (CFOSAT) [13], [25].

Figs. 7 and 8 present the modulation spectra of the range-resolved Doppler shifts [see (33)] and the weighted range-resolved Doppler shifts, i.e., $\widetilde{\psi}^0(x)\widetilde{f}_{GD}(x)/\psi^0$. In Figs. 7 and 8, black crosses represent the normalized spectrum of $\overline{\partial_t \eta_r}(x)$. For interpretation, we expand the

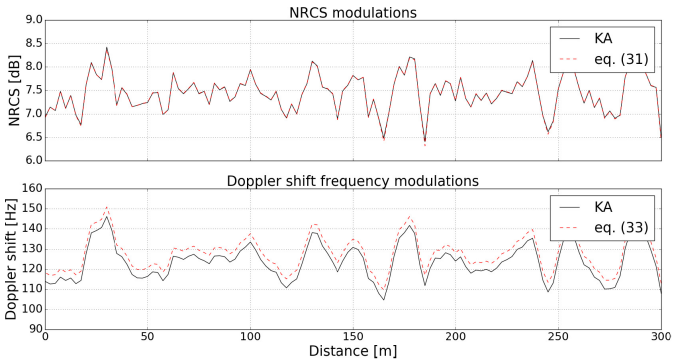

Fig. 5. Ka-band NRCS and Doppler shift frequency range modulations versus range distance at a 12° incidence radar. 8-m/s wind speed and 20-km long fetch Elfouhaily spectrum are considered. Solid curve is for Kirchhoff assumption (KA) and dashed curves are for approximations (31) and (33).

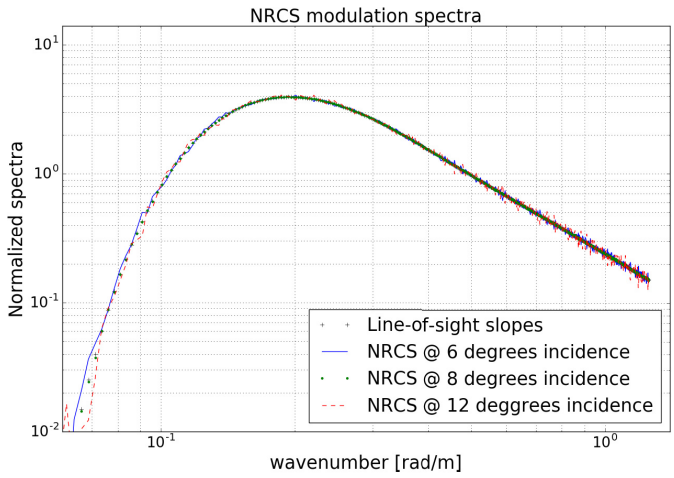

Fig. 6. Ka-band—normalized NRCS modulation spectra at 6°, 8°, and 12° incidence. LOS sea surface slope ($\overline{\partial_x \eta}(x)$) spectra are also superimposed.

weighted Doppler equation (33)

$$\frac{\widetilde{\psi}^0(x)\widetilde{f}_{GD}(x)}{(2\pi)^{-1}\psi^0} = Q_z \frac{\partial_{\tan\theta}\psi^0}{\psi^0}\mathrm{mss}_{\mathrm{xt}} - Q_z \frac{\partial_{\tan\theta}\psi^0}{\psi^0}\overline{\partial_x \eta_r}(x)\overline{\partial_t \eta_r}(x) + Q_z\overline{\partial_t \eta_r}(x) - Q_z \mathrm{mss}_{\mathrm{xt}}\overline{\partial_x \eta_r}(x)\frac{\partial^2_{\tan^2\theta}\psi^0}{\psi^0}. \tag{34}$$

On the right-hand side of (34), first line, we recognize the constant component of the mean Doppler shift, corrected by a negligible range-dependent term in the second line. The first term, third line, is the main modulation component directly proportional to the surface elevation velocity. Nonetheless, a correcting second term appears proportional to the curvature of the NRCS falloff with incidence. This term is also modulated and controlled by the LOS sea surface slopes. The amplitude and the sign of $\partial^2_{\tan^2\theta}\psi^0$ depend on the sea surface conditions and on the incidence angle, as shown in Fig. 9. Fig. 9 shows the incidence variations of ψ^0, $\partial_{\tan\theta}\psi^0/\psi^0$, and $\partial^2_{\tan^2\theta}\psi^0/\psi^0$.

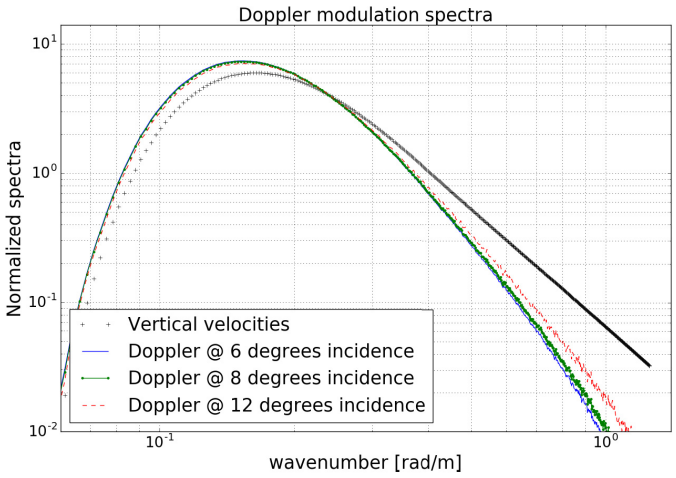

Fig. 7. Ka-band—normalized Doppler modulation spectra at 6°, 8°, and 12° incidence. LOS sea surface velocities ($\overline{\partial_t \eta(x)}$) spectra are also superimposed.

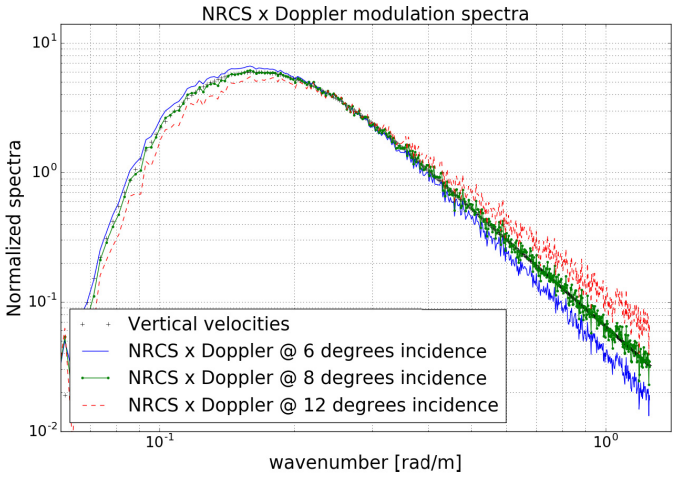

Fig. 8. Ka-band—normalized NRCS-weighted Doppler modulation spectra at 6°, 8°, and 12° incidence. LOS sea surface velocities ($\overline{\partial_t \eta(x)}$) spectra are also superimposed.

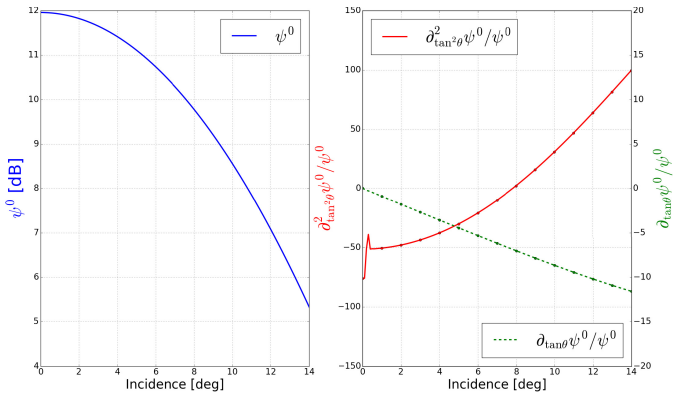

Fig. 9. Upwind incidence variations of ψ^0, $\partial_{\tan\theta}\psi^0/\psi^0$, and $\partial^2_{\tan^2\theta}\psi^0/\psi^0$ for the considered sea surface conditions: Elfouhaily spectrum with a 20-km fetch at a 8-m $\cdot$ s^{-1} wind speed.

For the considered sea conditions, the $\partial^2_{\tan^2\theta}\psi^0/\psi^0$ term vanishes around 8°. Consequently, at this particular incidence, velocity spectrum and weighted Doppler shift spectrum overlap (see Fig. 8).

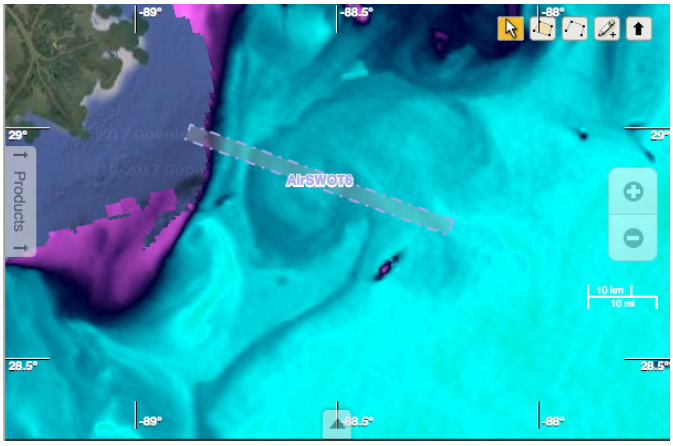

Fig. 10. AirSWOT flight #172803 on February 7, 2016 over the hammer-head mushroom seen by the VIIRS instrument (sea surface temperature).

For lower and higher incidences than this inversion zone, the modulation spectrum of the weighted Doppler exhibits higher and lower spectral slopes than the velocity spectrum.

For open-ocean conditions, more complex sea state conditions are expected [10], likely leading to a higher incidence inversion zone. As such, a radar operating between 8° and 12° incidence represents an optimal configuration to best cancel out this curvature correction and to help directly retrieve the surface velocity spectrum. As developed, range-resolved measurements thus provide joint-directional information for both radar intensity and Doppler measurements, to uniquely characterize the ambient sea state, i.e., directional spectral properties and kinematics.

IV. AirSWOT Data

The radar aboard Air Surface Water Ocean Topography (AirSWOT) (KaSPAR) is a Ka-band SAR sensor operated by the NASA Jet Propulsion Laboratory (JPL) flying aboard a King Air B200 aircraft operated by the NASA Armstrong Flight Research Center [26], [27]. The sensor gives access to NRCS and Doppler maps over the illuminated scene, which span from 0° to about 23° incidence covering a distance of about 4 km in the range direction for the flights considered in this paper. Both AirSWOT NRCS and SAR ATI Doppler data were processed and provided by the NASA Jet Propulsion Laboratory (JPL). Fig. 10 shows flight #172803 swath located over a "hammer-head" eddy, during the LAgrangian Submesoscale ExpeRiment (LASER) experiment [28]–[30] conducted in the Gulf of Mexico in January and February 2016.

Figs. 11 and 12 display radar intensity and Doppler maps sampled from the AirSWOT instrument, flight #172803 on February 7, 2017. As expected from the previous developments, joint modulations are clearly detected and plotted on Fig. 13. Ancillary data indicate surface wind speed of about 8 m $\cdot$ s^{-1}. Flight #172803 went from southeast to northwest, and the radar looked to the left, well aligned with the downwind/downwave direction, as shown in Fig. 12. The detected peak wavelength of 45 m corresponds to short fetch conditions.

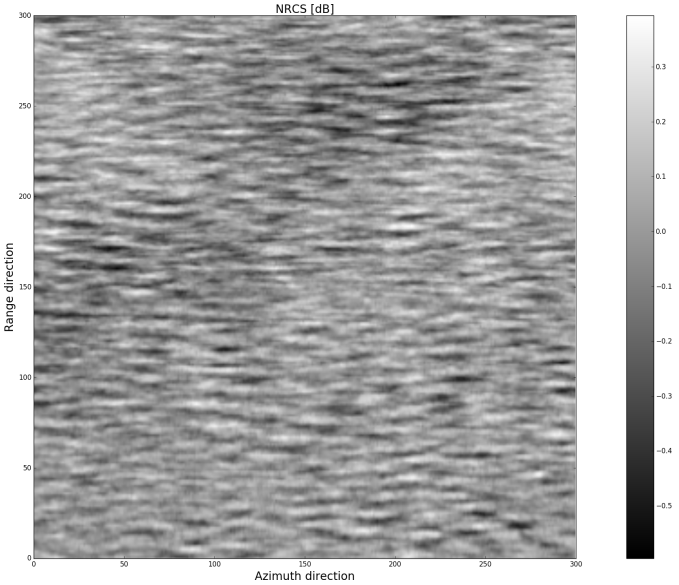

Fig. 11. Sample of NRCS modulations map observed with AirSWOT instrument on February 7, 2016 flight #172803.

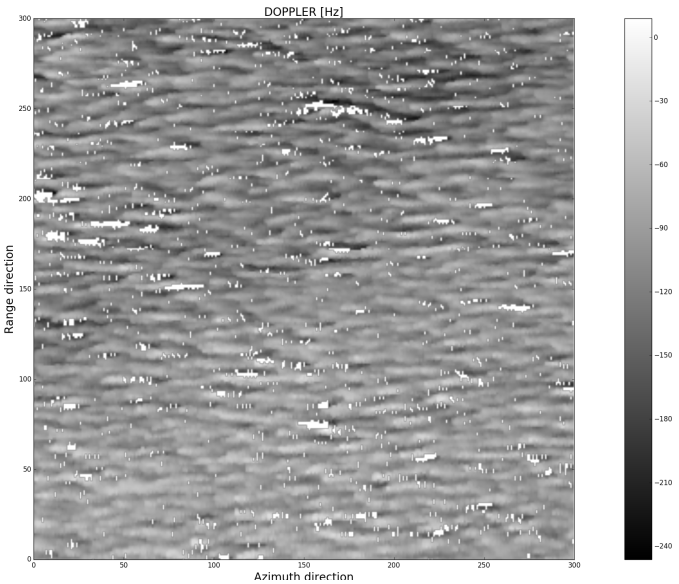

Fig. 12. Sample of Doppler modulations map observed with AirSWOT instrument on February 7, 2016 flight #172803.

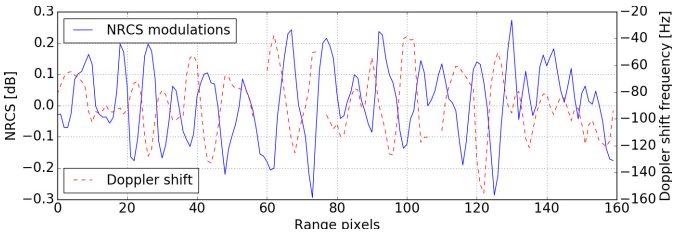

Fig. 13. Samples of NRCS and Doppler joint modulations transects in downwave looking configuration for AirSWOT flight #172803 on February 7, 2016.

Fig. 14 shows interpolated surface drifters velocity field at the time of the AirSWOT flight. Black lines are the swath boundaries. An along-track transect (red) of the AirSWOT Doppler map around the 12° incidence is marked in Fig. 15 as

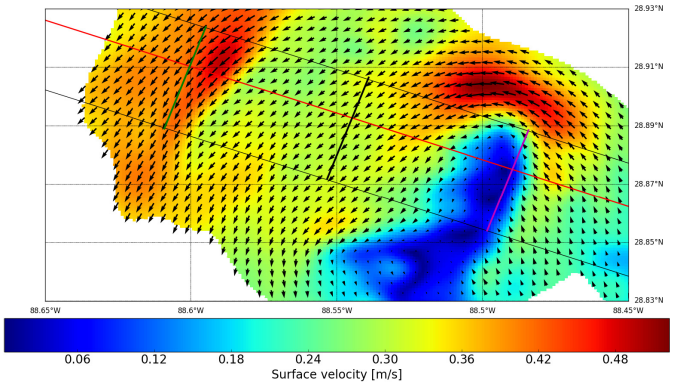

Fig. 14. Interpolated surface drifters velocity field colocated with AirSWOT flight #172803 on February 7, 2016. Colors indicates the *in situ* surface current velocity under the flight swath. Arrows indicates the surface current direction over the interpolated drifters area. Black lines are AirSWOT swath boundaries, and red line is the 12° incidence transect. Green, black, and magenta range transects are shown in Fig. 15 (top).

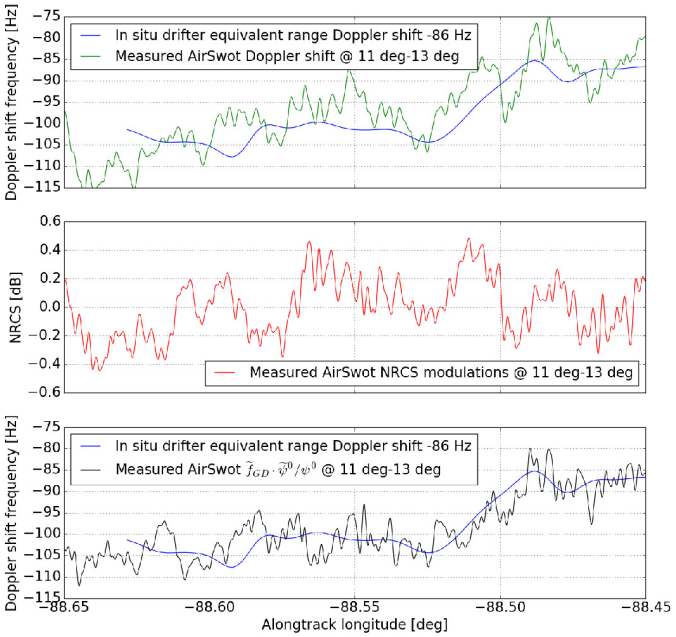

Fig. 15. (Top) Transect of Ka-band Doppler shift estimated from drifter velocities and measured by AirSWOT around 12° incidence. (Middle) Corresponding measured AirSWOT NRCS. (Bottom) Measured NRCS-weighted Doppler shift. Data were gathered during AirSWOT flight #172803 on February 7, 2016.

well as the corresponding *in situ* drifter velocity converted in LOS equivalent Ka-band Doppler shift (top). A mean negative shift has been added to take into account the Doppler wave bias in downwave looking conditions. It is adjusted to 86 Hz to scale the two curves. This bias, in principle, could be derived from a radar cross section fall-off analysis [see (15)]. Yet, inferring the wave bias from the NRCS also requires to know the $\mathrm{mss}_{\mathrm{xt}}$ parameter, which can only be derived from a diversity of azimuthal observations. This operation was not possible in this paper, as only upwave and downwave looking conditions were available.

The NRCS transect, corresponding to the 12° incidence, is also shown in Fig. 15 (middle). Fig. 15 (bottom) shows the weighted Doppler shift $\widetilde{f}_{\mathrm{GD}} \cdot \widetilde{\psi}^0/\psi^0$, where ψ^0 is the

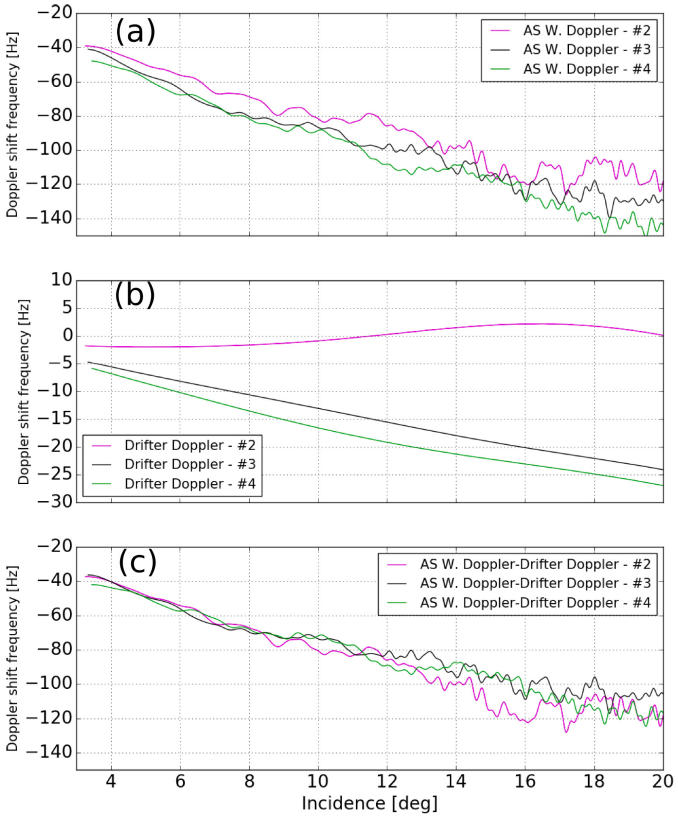

Fig. 16. (a) AS W.Doppler transects realized during flight #172803 and reported in Fig. 14. (b) *In situ* drifter Ka-band equivalent range Doppler shifts. (c) Difference of the top and middle panels. Remaining wave bias Doppler shifts of the three transects are superimposed meaning that wave conditions are similar.

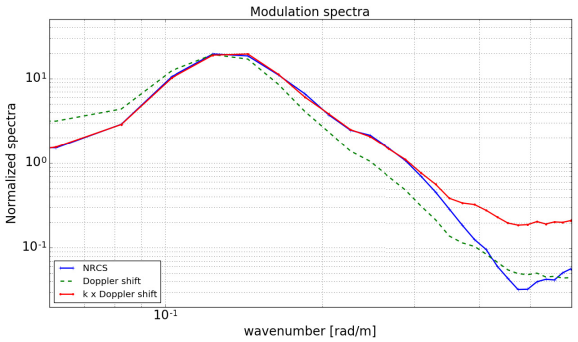

Fig. 17. AirSWOT range modulation NRCS and Doppler shift spectra. Modulation profiles between 11° and 13° incidence only are considered, and spectra are computed after a 400-m azimuthal averaging. The presented figure is the mean upwind spectra of AirSWOT flight #172803 on February 7, 2016.

mean magnitude of $\cos(12°)\sigma^0$ over the transect. The same drifter Doppler shift is also superimposed with an additional -86-Hz bias corresponding to the scaled weighted wave bias. Note, this bias corresponds to a 1.7-m $\cdot$ s^{-1} horizontal speed, which is about seven times larger than the local mean current speed. This clearly shows that an accurate knowledge of the ambient sea state is crucial to derive the underlying sea surface current. Nevertheless, the correspondence of the two measurements exemplifies the sensibility of a 12° incidence Ka-band Doppler radar to the sea surface current. Doppler and σ^0 range modulations can further be used to quantify this variability due to wave contribution and reduce current measurements uncertainties. From airborne geometry, modulations are obtained over a large range of incidence angles. Compared with the satellite geometry, for which the incidence angle is almost fixed, it hampers a direct application of (31) and (34). This is presently outside the scope of this paper and left for further studies.

Fig. 16(a) shows the variation of the AirSWOT weighted Doppler (AS W.Doppler) as a function of incidence for three locations during flight #172803 (transects are reported in Fig. 14) with very different current velocities. This again demonstrates the sensitivity of the measurements to the current velocity. Fig. 16(b) shows equivalent Ka-band range Doppler shifts derived from the drifters surface velocities along the same three transects. Fig. 16(c) presents the difference of the first two panels and is the remaining wave Doppler bias. All curves are well superimposed for the three different transects, and the local significant wave height variations (not shown here) explain, to first order, the remaining variability.

Still, Fig. 17 shows the good correspondence of the NRCS spectrum, that is proportional to k^2 times the elevation spectrum $E(k)$, and the Doppler spectrum, proportional to $kE(k)$ for deep water waves. The correspondence is particularly good around 12° incidence and consistent with our simple numerical test case in Fig. 8.

V. Conclusion

We have presented a theoretical framework for the analysis of Doppler measurements using a near-nadir radar instrument designed to measure sea surface velocities. The Kirchhoff approximation is used to derive and understand the basic concepts of radar sensor physics. Here, we focused on the SKIM satellite configuration, which can operate in Ka-band at 6° and 12° incidence [5].

From these analytical developments, an important conclusion is that 12°, in spite of a near-vertical geometry, is optimal for measuring time-varying waves in range-resolved measurements. This nontrivial conclusion comes from two results.

First, near-nadir configurations are favorable to infer directional wave properties (like SWIM instrument onboard CFOSAT). In particular, around 10°–12° incidence, the NRCS second derivative with respect to incidence vanishes, leading to linear relationships between the spectra of both NRCS and Doppler, and the spectrum of the sea surface elevation.

Second, up to 20° incidence in Ka-band, the expected LOS velocity is largely dominated by the correlation between surface orbital velocities and slopes, the msv parameter (as also found from platform Ka-band radar measurements [31]). This LOS velocity can reach up to 50 times the inherent Stokes drift.

Hence, with a range resolution of 3–5 m when projected on the ground, the measured NRCS and Doppler modulation spectra can thus give an accurate estimation of the msv. It then allows to estimate and correct the large wave-induced bias in the Doppler velocity to infer the surface current [5].

For coarser range resolutions, typically 30 m and more, the estimation of the msv would be less accurate and errors in retrieved surface currents larger.

These theoretical conclusions on the spectra of NRCS and Doppler and on the variation of the mean Doppler with incidence, wave, and currents are supported by the analysis of AirSWOT data operating in Ka-band from 0° to 23° incidence. A particular attention was paid on flight #172803 realized on February 7, 2016 in downwind/downwave conditions. As obtained, σ^0 and Doppler shift range modulations are clearly visible. Measured Doppler shifts combined with ground truth surface current velocities derived from local drifters deployed during LASER experiments further confirm the expected current impact on time-dependent measurements at near-nadir incidence.

This analysis clearly opens for new strategies to infer surface current information from precise ocean surface wave time-varying properties from satellite measurements.

APPENDIX

A. Elevation, Directional Spectrum, and Correlation Function

Without current, the linear random surface elevation η can be written

$$\eta(\boldsymbol{r},t)=\int_{\mathbb{R}^2} d\boldsymbol{k}\ a(\boldsymbol{k})e^{i(\boldsymbol{k}\cdot\boldsymbol{r}-\omega t)}+c.c. \tag{35}$$

where $a(\boldsymbol{k})$ is half the complex wave amplitude of wave $\boldsymbol{k}$ with random phase and $c.c.$ is the complex conjugate. It rewrites

$$\eta(\boldsymbol{r},t)=\int_{\mathbb{R}^2} d\boldsymbol{k}\ [a(\boldsymbol{k})e^{-i\omega t}+a^*(-\boldsymbol{k})e^{i\omega t}]e^{i\boldsymbol{k}\cdot\boldsymbol{r}}. \tag{36}$$

Assuming that η is a stationary process, the cross correlation $\rho(\boldsymbol{r}-\boldsymbol{r}',t-t')=\langle\eta(\boldsymbol{r},t)\eta(\boldsymbol{r}',t')\rangle$ writes

$$\rho(\boldsymbol{\xi},\tau)=\int_{\mathbb{R}^2} d\boldsymbol{k}[S_d(\boldsymbol{k})e^{-i\omega\tau}+S_d^*(-\boldsymbol{k})e^{i\omega\tau}]e^{i\boldsymbol{k}\cdot\boldsymbol{\xi}} \tag{37}$$

where $S_d(\boldsymbol{k})$ defined by $\langle a(\boldsymbol{k})a^*(\boldsymbol{k}')\rangle=S_d(\boldsymbol{k})\delta(\boldsymbol{k}-\boldsymbol{k}')$ is half the square amplitude of wave $\boldsymbol{k}$ and is real.

Note that S_d is the directive oceanic spectrum, which is not centrosymmetric. It follows that:

$$S(\boldsymbol{k})=S_d(\boldsymbol{k})+S_d(-\boldsymbol{k}) \tag{38}$$

is the well-known centrosymmetric spectrum.

Adding a horizontal current $\boldsymbol{U}$ [see (20)], we get

$$\eta_c(\boldsymbol{r},t)=\int_{\mathbb{R}^2} d\boldsymbol{k}\ [a(\boldsymbol{k})e^{-i\omega t}+a^*(-\boldsymbol{k})e^{i\omega t}]e^{i\boldsymbol{k}\cdot(\boldsymbol{r}-\boldsymbol{U}t)} \tag{39}$$

where subscript $_c$ accounts for current. The cross correlation $\rho_c(\boldsymbol{r}-\boldsymbol{r}',t-t')=\langle\eta_c(\boldsymbol{r},t)\eta_c(\boldsymbol{r}',t')\rangle$ writes

$$\rho_c(\boldsymbol{\xi},\tau)=\int_{\mathbb{R}^2} d\boldsymbol{k}[S_d(\boldsymbol{k})e^{-i\omega\tau}+S_d^*(-\boldsymbol{k})e^{i\omega\tau}]e^{i\boldsymbol{k}\cdot(\boldsymbol{\xi}-\boldsymbol{U}\tau)} \tag{40}$$

and we recognize

$$\rho_c(\boldsymbol{\xi},\tau)=\rho(\boldsymbol{\xi}-\boldsymbol{U}\tau,\tau). \tag{41}$$

B. Residual Modulation Statistics

Let us denotes by $(x,y)\mapsto f(x,y)$ the random function of interest, e.g. sea surface elevation, slope, velocity, and/or radar reflectivity modulation, with l_x and l_y, the correlation lengths along x and y, respectively, and $D=[-L_x/2,L_x/2]\times\left[-L_y/2,L_y/2\right]$ the bounded 2D intercepted domain. We also denote by

$$m_y(x)=\frac{1}{L_y}\int_{-\frac{L_y}{2}}^{\frac{L_y}{2}} dy\ f(x,y), \tag{42}$$

the residual, along y, mean profile of interest and

$$m=\frac{1}{L_xL_y}\iint_D dxdy\ f(x,y) \tag{43}$$

the mean of f. We can assume that $l_x\ll L_x$ and also that f is smooth and homogeneous. Accordingly, a covariance of f for $x-x'=\Delta x$ is defined as $C\left(\Delta x,(y-y')/l_y\right)$ and evaluated as

$$\frac{1}{L_x}\int_{-\frac{L_x}{2}}^{\frac{L_x}{2}} dx\ (f(x,y)-m_x(y))\left(f(x+\Delta x,y')-m_x(y')\right) \tag{44}$$

with

$$m_x(y)=\frac{1}{L_x}\int_{-\frac{L_x}{2}}^{\frac{L_x}{2}} du\ f(u,y). \tag{45}$$

The overall average, leading to estimate variance of the residual modulation, then writes:

$$\overline{C(\Delta x)}=\frac{1}{L_y^2}\int_{\left[-\frac{L_y}{2},\frac{L_y}{2}\right]^2} dydy'\ C\left(\Delta x,\frac{y-y'}{l_y}\right) \tag{46}$$

Considering $C\left(\Delta x,\frac{y-y'}{l_y}\right)\simeq 0$ for $y\neq y'$, we retrieve $\overline{C(\Delta x)}=\frac{1}{L_y}C(\Delta x,0)$, as previously suggested [11]. Not neglecting along-y correlation, the variance of the residual modulation becomes:

$$\overline{C(\Delta x)}=\left(\frac{l_y}{L_y}\right)\int_{-\frac{L_y}{l_y}}^{\frac{L_y}{l_y}} d\Delta y\ \left(1-|\Delta y|*\frac{l_y}{L_y}\right)C(\Delta x,\Delta y) \tag{47}$$

This general expression can then be analytically evaluated for specific covariance functions (e.g. Gaussian covariance). For the asymptotic case $l_y\ll L_y$, i.e. f not strongly correlated in the y direction, $\left(1-|\Delta y|*l_y/L_y\right)\approx 1$ (for bounded $|\Delta y|$). At large $|\Delta y|$, $C(0,\Delta y)$ rapidly decreases, leading to

$$\overline{C(\Delta x)}\approx\left(\frac{l_y}{L_y}\right)\int_{-\infty}^{\infty} d\Delta y\ C(\Delta x,\Delta y) \tag{48}$$

Depending on their directional covariance properties, i.e. distributed spectral directional spreads governing l_y, residual modulations thus further decreases with the azimuthal extent of the intercepted domain L_y. This development generalizes previous analyses [11], explicitly introducing the previously omitted, l_y dependency.

ACKNOWLEDGMENT

The authors would like to thank the NASA Jet Propulsion Laboratory and in particular E. Rodriguez for discussions and provision of the data. The interpolated LASER drifter velocity field was provided by R. Goncalves at RSMAS. Part of the research was carried out at the Jet Propulsion Laboratory, California Institute of Technology, under a contract with the National Aeronautics and Space Administration.

REFERENCES

[1] B. Chapron, F. Collard, and F. Ardhuin, "Direct measurements of ocean surface velocity from space: Interpretation and validation," *J. Geophys. Res.*, vol. 110, no. C7, pp. 0148–0227, 2005.

[2] A. A. Mouche, B. Chapron, N. Reul, and F. Collard, "Predicted Doppler shifts induced by ocean surface wave displacements using asymptotic electromagnetic wave scattering theories," *Waves Random Complex Media*, vol. 18, no. 1, pp. 185–196, 2008.

[3] F. Nouguier, C.-A. Guéri, and G. Soriano, "Analytical techniques for the Doppler signature of sea surfaces in the microwave regime—I: Linear surfaces," *IEEE Trans. Geosci. Remote Sens.*, vol. 49, no. 12, pp. 4856–4864, Dec. 2011.

[4] G. Caudal, D. Hauser, R. Valentin, and C. L. Gac, "KuROS: A new airborne Ku-band Doppler radar for observation of surfaces," *J. Atmos. Ocean. Technol.*, vol. 31, no. 10, pp. 2223–2245, 2014.

[5] F. Ardhuin *et al.*, "Measuring currents, ice drift, and waves from space: The Sea Surface KInematics Multiscale monitoring (SKIM) concept," *Ocean Sci.*, vol. 14, pp. 337–354, 2018, [Online]. Available: https://doi.org/10.5194/os-14-337-2018

[6] M. Hansen *et al.*, "Simulation of radar backscatter and Doppler shifts of wave–current interaction in the presence of strong tidal current," *Remote Sens. Environ.*, vol. 120, pp. 113–122, May 2012.

[7] R. Romeiser, H. Runge, S. Suchandt, R. Kahle, C. Rossi, and P. S. Bell, "Quality assessment of surface current fields from TerraSAR-X and TanDEM-X along-track interferometry and Doppler centroid analysis," *IEEE Trans. Geosci. Remote Sens.*, vol. 52, no. 5, pp. 2759–2772, May 2014.

[8] A. C. H. Martin, C. Gommenginger, J. Marquez, S. Doody, V. Navarro, and C. Buck, "Wind-wave-induced velocity in ATI SAR ocean surface currents: First experimental evidence from an airborne campaign," *J. Geophys. Res. Oceans*, vol. 121, no. 3, pp. 1640–1653, Mar. 2016.

[9] P. Beckmann and A. Spizzichino, *The Scattering of Electromagnetic Waves From Rough Surfaces*. Norwood, MA, USA: Artech House, 1987, p. 511.

[10] F. Nouguier, A. Mouche, N. Rascle, B. Chapron, and D. Vandemark, "Analysis of dual-frequency ocean backscatter measurements at ku- and Ka-bands using near-nadir incidence GPM radar data," *IEEE Geosci. Remote Sens. Lett.*, vol. 13, no. 9, pp. 1310–1314, Sep. 2016.

[11] F. C. Jackson, "An analysis of short pulse and dual frequency radar techniques for measuring ocean wave spectra from satellites," *Radio Sci.*, vol. 16, no. 6, pp. 1385–1400, 1981.

[12] F. C. Jackson, "The radar ocean-wave spectrometer," *Johns Hopkins APL Tech. Dig.*, vol. 8, no. 1, pp. 116–127, 1987.

[13] D. Hauser, C. Tison, T. Amiot, L. Delaye, N. Corcoral, and P. Castillan, "SWIM: The first spaceborne wave scatterometer," *IEEE Trans. Geosci. Remote Sens.*, vol. 55, no. 5, pp. 3000–3014, May 2017.

[14] D. Thompson, B. Gotwols, and W. Keller, "A comparison of k_u-band Doppler measurements at 20° incidence with predictions from a time-dependent scattering model," *J. Geophys. Res., Oceans*, vol. 96, no. C3, pp. 4947–4955, 1991.

[15] T. Elfouhaily, S. Guignard, R. Awadallah, and D. R. Thompson, "Local and non-local curvature approximation: A new asymptotic theory for wave scattering," *Waves Random Media*, vol. 13, no. 4, pp. 321–337, 2003, doi: https://doi.org/10.1088/0959-7174/13/4/308

[16] T. Elfouhaily, B. Chapron, K. Katsaros, and D. Vandemark, "A unified directional spectrum for long and short wind-driven waves," *J. Geophys. Res., Oceans*, vol. 102, no. C7, p. 15781–15796, 1997.

[17] N. Tran and B. Chapron, "Combined wind vector and sea state impact on ocean nadir-viewing Ku- and C-band radar cross-sections," *Sensors*, vol. 6, no. 3, pp. 193–207, 2006.

[18] Y. Quilfen, B. Chapron, A. Bentamy, J. Gourrion, T. E. Fouhaily, and D. Vandemark, "Global ERS 1 and 2 and NSCAT observations: Upwind/crosswind and upwind/downwind measurements," *J. Geophys. Res., Oceans*, vol. 104, no. C5, p. 11 459–11 469, 1999.

[19] E. Walsh *et al.*, "The southern ocean waves experiment. Part III: Sea surface slope statistics and near-nadir remote sensing," *J. Phys. Oceanograp.*, vol. 38, no. 3, pp. 670–685, 2008.

[20] *Global Precipitation Measurement*. Accessed: Sep. 2017. [Online]. Available: http://www.nasa.gov/gpm

[21] J. A. Johannessen *et al.*, "Direct ocean surface velocity measurements from space: Improved quantitative interpretation of Envisat ASAR observations," *Geophys. Res. Lett.*, vol. 35, no. 22, pp. 1–6, 2008.

[22] M. J. Rouault, A. Mouche, F. Collard, J. A. Johannessen, and B. Chapron, "Mapping the Agulhas Current from space: An assessment of ASAR surface current velocities," *J. Geophys. Res.*, vol. 41, C10, pp. 1–14, 2010.

[23] A. A. Mouche *et al.*, "On the use of Doppler shift for sea surface wind retrieval from SAR," *IEEE Trans. Geosci. Remote Sens.*, vol. 50, no. 7, pp. 2901–2909, Jul. 2012.

[24] F. Nouguier, C.-A. Guérin, and B. Chapron, "'Choppy wave' model for nonlinear gravity waves," *J. Geophys. Res., Oceans*, vol. 114, no. C9, pp. 1–16, 2009.

[25] F. C. Jackson, "The reflection of impulses from a nonlinear random sea," *Radio Sci.*, vol. 16, no. 6, pp. 1385–1400, 1981.

[26] *Airswot Description*. Accessed: Sep. 2017. [Online]. Available: https://swot.jpl.nasa.gov/airswot/

[27] D. Moller, E. Rodriguez, J. Carswell, and D. Esteban-Fernandez, "Airswot—A calibration/validation platform for the SWOT mission," in *Proc. Int. Geosci. Remote Sens. Symp.*, Vancouver, BC, Canada, Jul. 2011.

[28] E. H. Altenau *et al.*, "AirSWOT measurements of river water surface elevation and slope: Tanana River, AK," *Geophys. Res. Lett.*, vol. 44, no. 1, pp. 181–189, 2017.

[29] N. Rascle, J. Molemaker, L. Marié, F. Nouguier, B. Chapron, B. Lund, and A. Mouche, "Intense deformation field at oceanic front inferred from directional sea surface roughness observations," *Geophys. Res. Lett.*, vol. 44, no. 11, pp. 5599–5608, 2017.

[30] E. A. D'Asaro *et al.*, "Ocean convergence and the dispersion of flotsam," *Proc. Nat. Acad. Sci. USA*, vol. 115, no. 11, p. E2664, 2018. [Online]. Available: http://www.pnas.org/content/115/11/E2664, doi: 10.1073/pnas.1802701115.

[31] Y. Y. Yurovsky, V. N. Kudryavtsev, B. Chapron, and S. A. Grodsky, "Modulation of Ka-band Doppler radar signals backscattered from the sea surface," *IEEE Trans. Geosci. Remote Sens.*, vol. 56, no. 5, pp. 2931–2948, May 2018.

Frédéric Nouguier received the Agrégation and M.S. degrees in applied physics from the Ecole Normale Supérieure de Cachan, Cachan, France, the M.S. degree in physical methods for remote sensing from the University of Paris-Diderot, Paris, France, and the Ph.D. degree in physics from Aix-Marseille University, Marseille, France, in 2009.

He is currently a Research Scientist with the Laboratoire d'Océanographie Physique et Spatiale, Institut Francais de Recherche pour l'Exploitation de la Mer, Plouzané, France. He has experience in applied mathematics, physical oceanography, and electromagnetic wave theory and its application to ocean remote sensing.

Bertrand Chapron received the B.Eng. degree from the Institut National Polytechnique de Grenoble, Grenoble, France, in 1984, and the Ph.D. degree in physics (fluid mechanics) from the University of Aix-Marseille II, Marseille, France, in 1988.

He spent three years as a Post-Doctoral Research Associate with the NASA Goddard Space Flight Center, Greenbelt, MD, USA, and the Wallops Flight Facility, Wallops Island, VA, USA. He is currently a Research Scientist with the Laboratoire d'Océanographie Physique et Spatiale, Institut Francais de Recherche pour l'Exploitation de la Mer, Plouzané, France. He has experience in applied mathematics, physical oceanography, and electromagnetic wave theory and its application to ocean remote sensing.

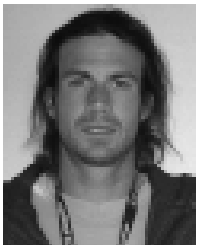

Fabrice Collard graduated in off-shore engineering from the Ecole Centrale de Lyon, Lyon, France, in 1996, and the Ph.D. degree in oceanography, meteorology and environment from the University of Paris VI, Paris, France, in 2000. His thesis was dedicated to the 3-D aspect of wind–wave field.

He was a Post-Doctoral Research Associate in HF radars at the Rosenstiel School of Marine and Atmospheric Science, Miami, FL, USA, from 2000 to 2001. He was with the Spatial Oceanography Laboratory, Institut Francais de Recherche pour l'Exploitation de la Mer, Plouzané, France, in 2002, where he was involved in the validation of the synthetic aperture radar wave mode products of ENVISAT. He was a Research Engineer at BOOST-Technologies, Plouzané, in 2003 and 2008 and the Head of research and development activities at the Radar Application Division, Collecte Localisation Satellites, Plouzané, from 2008 to 2013, where he has been involved in the development of algorithms and prototypes for operational wind wave and current applications. He is currently the President of OceanDataLab, Locmaria-Plouzané, France, where he is involved in ocean remote sensing multisensor synergy methods and tools.

Alexis A. Mouche received the Ph.D. degree in ocean remote sensing from the Université de Versailles Saint-Quentin-en-Yvelines, Versailles, France, in 2005.

He has been a permanent position with the Laboratoire d'Océanographie Physique et Spatiale, Institut Francais de Recherche pour l'Exploitation de la Mer, Plouzané, France, since 2014. His research interests include the interaction of electromagnetic and oceanic waves for ocean remote sensing applications.

Nicolas Rascle graduated from ENSTA ParisTech, Paris, France, in 2004, and the Ph.D. degree from the University of Western Brittany, Brest, France, in 2007.

He spent three years as a Post-Doctoral Research Associate with the University of Cape Town, Cape Town, South Africa. He was a Research Associate with the Institut Francais de Recherche pour l'Exploitation de la Mer, Plouzané, France, from 2012 to 2017. He was mainly involved in the impact of waves on the air–sea interface (turbulence, surface currents, and wave–current interactions). He is specialized in wave dynamics. He is also specialized in the role of waves and surface roughness for the remote sensing of wind, waves, and currents.

Fabrice Ardhuin graduated from Ecole Polytechnique, Palaiseau, France, in 1997, and the Ph.D. degree in oceanography from the U.S. Naval Postgraduate School, Monterey, CA, USA, in 2001.

He has been involved in ocean waves and related topics, from microseisms to remote sensing, with a strong focus on wave-current and wave-ice interactions, first at the French Navy Hydrographic and Oceanographic Service, Brest, France, then Institut Francais de Recherche pour l'Exploitation de la Mer, Plouzané, France, and recently CNRS. He is currently the Chairman of Laboratoire d'Océanographie Physique et Spatiale, Institut Francais de Recherche pour l'Exploitation de la Mer, a member of the SWOT Science Team, and a Principal Investigator for the surface kinematics multiscale proposal.

Xiaoqing Wu received the B.S. and M.S. degrees in electrical engineering from the Nanjing University of Aeronautics and Astronautics, Nanjing, China, in 1982 and 1985, respectively, and the Ph.D. degree in electrical engineering from the University of Stuttgart, Stuttgart, Germany, in 1998.

He was involved in the data system design and development for the Modified Antarctic Mapping Mission and contributed to producing the first Antarctic surface velocity map and the interferometric coherence map, while he was a Senior Research Engineer with Vexcel Corporation, Boulder, CO, USA, from 1998 to 2008, where he has been involved in radar ice sounding since 2005. He joined the Jet Propulsion Laboratory, California Institute of Technology, Pasadena, CA, USA, in 2008, and has produced the first radar image of Greenland ice sheet bed. He has also been involved in NASA's SWOT mission and Glistin and AirSWOT projects with extensive experiences in SAR data processing and analysis. His research interests include synthetic aperture radar (SAR) processing algorithms, interferometry, SAR tomography, and radar ice sounding.